Chemical evolution of fluorine in the Milky Way

Kate A. Womack [1]★ Fiorenzo Vincenzo [1] Brad K. Gibson,[1] Benoit Côté [2,3] Marco Pignatari,[1,3,4]
Hannah E. Brinkman,[3,5,6] Paolo Ventura [7,8] and Amanda Karakas [9,10]

[1]*E. A. Milne Centre for Astrophysics, University of Hull, Hull HU6 7RX, UK*

[2]*Department of Physics and Astronomy, University of Victoria, Victoria, BC V8P 5C2, Canada*

[3]*Konkoly Observatory, Research Centre for Astronomy and Earth Sciences, H-1121 Budapest, Hungary*

[4]*NuGrid Collaboration*

[5]*Institute of Astronomy, KU Leuven, Celestijnenlaan 200D, B-3001 Leuven, Belgium*

[6]*Graduate School of Physics, University of Szeged, Dom tér 9, H-6720 Szeged, Hungary*

[7]*INAF, Observatory of Rome, Via Frascati 33, I-00077 Monte Porzio Catone, Italy*

[8]*Instituto Nazionale di Fisica Nucleare, Section of Perugia, Via A. Pascoli snc, I-06123 Perugia, Italy*

[9]*School of Physics and Astronomy, Monash University, Clayton, VIC 3800, Australia*

[10]*ARC Centre of Excellence for All Sky Astrophysics in 3 Dimensions (ASTRO-3D), Clayton 3800, Australia*

ABSTRACT

Fluorine has many different potential sites and channels of production, making narrowing down a dominant site of fluorine production particularly challenging. In this work, we investigate which sources are the dominant contributors to the galactic fluorine by comparing chemical evolution models to observations of fluorine abundances in Milky Way stars covering a metallicity range of $-2 <$ [Fe/H] < 0.4 and upper limits in the range of $-3.4 <$ [Fe/H] < -2.3. In our models, we use a variety of stellar yield sets in order to explore the impact of varying both asymptotic giant branch (AGB) and massive star yields on the chemical evolution of fluorine. In particular, we investigate different prescriptions for initial rotational velocity in massive stars as well as a metallicity-dependent mix of rotational velocities. We find that the observed [F/O] and [F/Fe] abundance ratios at low metallicity and the increasing trend of [F/Ba] at [Fe/H] $\gtrsim -1$ can only be reproduced by chemical evolution models assuming, at all metallicities, a contribution from rapidly rotating massive stars with initial rotational velocities as high as 300 km s^{-1}. A mix of rotational velocities may provide a more physical solution than the sole use of massive stars with $v_{\rm rot} = 300$ km s^{-1}, which are predicted to overestimate the fluorine and average s-process elemental abundances at [Fe/H] $\gtrsim -1$. The contribution from AGB stars is predicted to start at [Fe/H] ≈ -1 and becomes increasingly important at high metallicity, being strictly coupled to the evolution of the nitrogen abundance. Finally, by using modern yield sets, we investigate the fluorine abundances of Wolf–Rayet winds, ruling them out as dominant contributors to the galactic fluorine.

Key words: stars: abundances – Galaxy: abundances – Galaxy: disc – Galaxy: evolution.

1 INTRODUCTION

For many years, understanding the origin and evolution of fluorine has posed a challenge for the scientific community. Fluorine has just one stable isotope, ^{19}F, with many different channels of production depending on the conditions in stars. ^{19}F is also fragile and can be easily destroyed by α-captures (e.g. Meynet & Arnould 2000). This makes narrowing down a dominant site for fluorine production particularly difficult. There are five main sites that frequently appear in the literature as having the potential to contribute significantly to the chemical evolution of fluorine; these are the following:

(i) *Asymptotic giant branch (AGB) stars***:** Fluorine is produced in AGB stars during thermal pulses (Forestini et al. 1992; Straniero, Gallino & Cristallo 2006). Secondary ^{19}F is made from ^{14}N seed nuclei via the following two chains of reactions: ^{14}N (n, p)^{14}C$(\alpha, \gamma)^{18}$O (p, α)^{15}N $(\alpha, \gamma)^{19}$F and ^{14}N$(\alpha, \gamma)^{18}$F$(\beta^+)^{18}$O(p,

α)^{15}N$(\alpha, \gamma)^{19}$F (Lugaro et al. 2004). In certain conditions, primary fluorine can also be made in AGB stars from the rapid burning of ^{13}C at high temperatures, which produces ^{15}N and allows for the nucleosynthesis of fluorine via ^{15}N $(\alpha, \gamma)^{19}$F (Cristallo et al. 2014). For a more detailed review of the ^{19}F production channels in AGB stars, see Lucatello et al. (2011). Kobayashi, Karakas & Umeda (2011a) found that the dominant AGB mass range for fluorine production is 2–4 M$_\odot$, over which temperatures do not get hot enough for hot bottom burning to occur, preventing the destruction of fluorine via ^{19}F $(\alpha,$ p) ^{22}Ne. However, it should be noted that the yield set used in Kobayashi et al. (2011a) favours ^{19}F production in this mass range (see fig. 8 of Karakas & Lattanzio 2007). There is observational evidence that AGB stars contribute to the galactic fluorine (see the pioneering works of Jorissen, Smith & Lambert 1992). However, it is still unclear whether AGB stars can account for the total galactic abundance of fluorine.

(ii) *Wolf–Rayet (WR) stars*: Fluorine can be produced by WR stars during the helium burning phase. Again, the seed nuclei for ^{19}F production in these stars are ^{14}N. If the ^{14}N is of secondary

* E-mail: k.a.womack-2017@hull.ac.uk

origin, then the behaviour of ^{19}F is also secondary and is therefore metallicity dependent. It is thought that WR winds can eject some of the fluorine before it is destroyed by α-captures; this process is the result of a delicate balance between the rate at which mass is lost via winds and the efficiency of the ^{19}F (α, p) ^{22}Ne reaction. In one of their models, Meynet & Arnould (2000) predicted that WR stars can produce as much as 2×10^{-3} M$_\odot$ of ^{19}F. However, since then other studies have revealed that the ^{19}F yield in massive star winds may not be as high as this (e.g. Palacios, Arnould & Meynet 2005; Stancliffe et al. 2005; Brinkman 2022). For example, when rotation is accounted for, Palacios et al. (2005) found that the WR fluorine yield falls significantly with respect to Meynet & Arnould (2000). Interestingly, Brinkman (2022) found negative net yields of ^{19}F in all their rotating and non-rotating models, with the exception of an 80 M$_\odot$ model with an initial rotational velocity $v_{rot} = 150$ km s^{-1}. All this raises the question – do WR stars contribute to the galactic fluorine budget at all, which will be addressed in later sections of this work.

(iii) *Rotating massive stars*: Fluorine can be produced in massive stars in the He convective shell via the series of reactions ^{14}N (α, γ) ^{18}F (β^+) ^{18}O (p, α) ^{15}N (α, γ) ^{19}F (Goriely, Jorissen & Arnould 1989; Choplin et al. 2018). This chain of reactions becomes enhanced when rotation is induced, due to the increased abundance of CNO elements that arises as a result of rotation (Limongi & Chieffi 2018).

(iv) *Core-collapse supernovae (CCSNe)*: The ν-process in CCSNe is also a proposed site for fluorine production (Woosley & Haxton 1988; Kobayashi et al. 2011b). CCSNe are powered by neutrino heating mechanisms. These neutrinos can interact with some nuclides, including fluorine. ^{19}F is produced via the ν-process in CCSNe by the following reaction: ^{20}Ne $(\nu, \nu' p)^{19}$F. Exactly how much fluorine this process might produce in CCSNe is unclear because there is uncertainty around the flux and energy of the neutrinos. However, given that this production is a primary process, more observations at low metallicity might help us to constrain how much fluorine we might expect to be produced by this source.

(v) *Novae*: Jose & Hernanz (1998) showed that fluorine can be produced by novae. The mechanism for novae to produce fluorine is as follows: ^{17}O (p, γ) ^{18}F (p, γ) ^{19}Ne (β^+) ^{19}F. Just as with the ν-process, fluorine yields from novae are still highly uncertain. Jose & Hernanz (1998) found that fluorine was only significantly synthesized in their 1.35 M$_\odot$ models. Therefore, we cannot be sure of their contribution to the galactic fluorine abundance.

Note that here and throughout this work we define AGB stars in the mass range $1 \leq M/M_\odot \leq 8$ and massive stars $8 < M/M_\odot \leq 120$.

Many chemical evolution studies have tried to disentangle this web and figure out which sources of fluorine are dominant in different metallicity ranges. There is not much agreement between authors. Renda et al. (2004) used the WR yields of Meynet & Arnould (2000) to show that WR stars can dominate fluorine production at solar and supersolar metallicities, while AGB stars were required in their models to reproduce the trends at lower metallicities. This is in contrast to the work of Olive & Vangioni (2019), who concluded that AGB stars dominate at high metallicity and that the ν-process in CCSNe is required to reproduce low-metallicity observations. A combination of AGB stars and neutrino process was also used by Kobayashi et al. (2011b) to reproduce the observed behaviour of [F/O] in globular cluster and solar neighbourhood stars.

Timmes, Woosley & Weaver (1995) was the first chemical evolution study to investigate fluorine, and they found that the inclusion of novae can reproduce [F/O] ratios in combination with AGB stars. The need for novae to reproduce [F/O] versus [O/H] ratios was

also found by Spitoni et al. (2018), who concluded that AGB and WR stars dominate galactic fluorine production. We note again that Kobayashi et al. (2011a) found that the dominant AGB mass range that contributes to fluorine is 2–4 M$_\odot$ but this contribution can only be seen at [Fe/H] $\gtrsim -1.5$ dex.

By assuming that massive stars have, on average, increasingly faster initial rotational velocities at low metallicities, Prantzos et al. (2018) found that rotating massive stars can dominate the evolution of fluorine in the solar neighbourhood up to solar metallicity. A similar conclusion was reached by Grisoni et al. (2020), who investigated the chemical evolution of fluorine by separately modelling the thick and thin discs of the Milky Way using the so-called parallel model of Grisoni et al. (2017). In particular, Grisoni et al. (2020) concluded that rotating massive stars can dominate fluorine production up to solar metallicity but a boost in fluorine is also needed at higher metallicities in order to match the behaviour of the observations. They proposed that this boost could be obtained either by artificially enhancing the AGB yields or by including an additional contribution from novae in the models. The prescription for rotating massive stars in Grisoni et al. (2020) follows the assumptions of Romano et al. (2019) where all stars with [Fe/H] < -1 dex are given an initial rotational velocity $v_{rot} = 300$ km s^{-1}, while all stars with [Fe/H] ≥ -1 dex have $v_{rot} = 0$ km s^{-1}. Rotating massive stars were first recognized as important at low metallicity by Chiappini et al. (2006) in relation to primary nitrogen production, which is the seed for fluorine production. This arose from the work of Matteucci (1986), who recognized the need for another primary component of nitrogen.

Fluorine has also recently become an element of interest for high redshift studies. Franco et al. (2021) were able to estimate the abundance of fluorine in a gravitationally lensed galaxy at a redshift (z) of 4.4, determining that WR stars must be responsible for the observed fluorine abundance enhancement. Though this is not a Milky Way observation, it can still give us an idea of the origins of fluorine in the early Universe and thus, presumably, at low metallicity.

Aside from the uncertainties in the dominant production site of fluorine, we must also contend with difficulty in gathering observations of fluorine. The majority of fluorine abundance determinations in the literature are obtained from the analysis of ro-vibrational HF lines at 2.3 μm (Abia et al. 2015). This spectral range is contaminated by lots of telluric lines, which prevent the use of many HF lines for fluorine abundance determinations. Recently, the first detection of an AlF line was obtained in 2 M-type AGB stars (Saberi et al. 2022). Danilovich et al. (2021) also detected the AlF line towards an S-type AGB star, measuring an abundance of AlF 40 per cent greater than solar.

Most fluorine observations for chemical evolution studies are available using HF lines as detected in both galactic and extragalactic AGB stars (Abia et al. 2011, 2015, 2019), field stars (Lucatello et al. 2011; Li et al. 2013), and in the Galactic Centre (Guerço et al. 2022). There are also a variety observations of fluorine in open and globular clusters (e.g. Cunha et al. 2003; Cunha & Smith 2005; Smith et al. 2005; Yong et al. 2008; de Laverny & Recio-Blanco 2013; Nault & Pilachowski 2013; Maiorca et al. 2014). Since this work is mainly focused on the chemical evolution of fluorine in Milky Way field stars, the previously listed observations in open and globular clusters will not be included in our analysis.

The evolution of fluorine at low metallicity (e.g. [Fe/H] $\lesssim -1.5$ dex) poses a particular challenge because of a large contamination from telluric lines and blending of the HF lines with CO features (Lucatello et al. 2011). Despite those

challenges, there are some measurements of fluorine abundances at low metallicities, which include a sample of red giants from Lucatello et al. (2011) and two red giants in the Carina dwarf spheroidal (dSph) galaxy from Abia et al. (2015) among others (e.g. Li et al. 2013; Mura-Guzmán et al. 2020). Both the stellar sample of Lucatello et al. (2011) and the Carina stars from Abia et al. (2015) are considered in our work.

The structure of the paper is as follows: Section 2 lays out the sample of fluorine abundance measurements that are used in this work for different metallicity ranges, Section 3 introduces the main hypothesis and working assumptions of our galactic chemical evolution (GCE) model and summarizes the different combinations of yields that are included in the model, Section 4 presents the main chemical evolution trends of interest as predicted by our model to reproduce observational data, and Section 5 explains how these results can help us to probe the chemical evolution of fluorine. Finally, in Section 6, we present our conclusions.

2 OBSERVATIONS

The most recent set of fluorine abundance measurements is those of Ryde et al. (2020), who observed 66 red giants using the Immersion GRating INfrared Spectrometer and the *Phoenix* infrared high-resolution spectrograph at the Gemini South Observatory. The metallicity range of these observations is $-1.1 <$ [Fe/H] < 0.4, which extends the metallicity range of fluorine abundances in the solar neighbourhood that were available previous to this study (e.g. Jönsson et al. 2017).

Due to telluric lines and blending, much of the data we have at low [Fe/H] are upper limits rather than absolute measurements. Though not as conclusive as absolute measurements, upper limits can still tell us about the range of fluorine abundances we might expect and can give us a preliminary idea of whether our chemical evolution models can reproduce observations at low metallicity. The primary set of fluorine observations at low metallicity used in this work consists of a sample of 11 metal-poor red giant stars from Lucatello et al. (2011). The abundances were measured from the analysis of spectra obtained with the CRyogenic high-resolution InfraRed Echelle Spectrograph on the European Southern Observatory's Very Large Telescope (VLT). Of the 11 stars in the metallicity range $-3.4 <$ [Fe/H] < -1.3, two have abundance measurements of fluorine, while the remaining nine have upper limits provided.

Eight red giants in the sample of Lucatello et al. (2011) are classified as CEMP-s stars (carbon-enhanced metal-poor stars that are also enriched in s-process elements), whereas two stars are classified as CEMP-no star (not enriched with s-process or r-process elements). There is also one star in this sample classified as carbon normal. While the physical origin of CEMP-no stars is still unclear and debated (Aoki et al. 2002; Hansen et al. 2016a; Yoon et al. 2016), the s-process and carbon enhancement as measured in the atmosphere of CEMP-s red giants likely results from binary mass transfer from an AGB companion that changed the initial surface abundances (e.g. Beers & Christlieb 2005; Lucatello et al. 2005; Bisterzo et al. 2010; Lugaro et al. 2012; Starkenburg et al. 2014; Hampel et al. 2016; Hansen et al. 2016b). Therefore, the predictions of our chemical evolution models at low [Fe/H] solely provide a baseline for the average fluorine abundances at birth in CEMP-s red giants before mass transfer took place. We also include fluorine measurements as obtained in two stars of the Carina dSph galaxy by Abia et al. (2015). These measurements were obtained from spectra taken using the *Phoenix* infrared high-resolution spectrograph by Abia et al. (2011) and reanalysed by using the spectral synthesis code TERBOSPECTRUM

by Abia et al. (2015). The formation of Carina occurred with low star formation efficiencies and a short infall time-scale (e.g. Lanfranchi, Matteucci & Cescutti 2006; Vincenzo et al. 2014), as did the Milky Way halo. Therefore, observations in Carina dSph have been included in this work in order to further our understanding of how fluorine might behave at low metallicity in general. However, since these stars are not Milky Way stars we must be careful as they are not directly comparable with the chemical evolution models presented in this work or the other observations. The chemical evolution of fluorine in Carina will be the subject of future work.

3 GALACTIC CHEMICAL EVOLUTION MODEL

We have used the chemical evolution code OMEGA+[1] (Côté et al. 2018). This is a two-zone model where a central star-forming region is modelled using the code OMEGA[2] (Côté et al. 2017), which simulates the evolution of several physical and chemical properties within a cold gas reservoir, surrounded by a non-star-forming hot gas reservoir. The latter is considered as the circumgalactic medium (CGM) in our model.

We can follow both the evolution of the CGM and the internal star-forming galaxy. The evolution of the mass of the gas in the CGM (M_{CGM}) is as follows:

$$\dot{M}_{CGM}(t) = \dot{M}_{CGM,in}(t) + \dot{M}_{outflow}(t) - \dot{M}_{inflow}(t) - \dot{M}_{CGM,out}(t), \quad (1)$$

where $\dot{M}_{CGM,in}$ is the inflow rate from the external intergalactic medium into the CGM, $\dot{M}_{outflow}$ is the mass removed from the central galaxy and added to the CGM via outflow, $\dot{M}_{inflow}$ is the gas that flows into the galaxy from the CGM, and $\dot{M}_{CGM,out}$ is the outflow rate of gas from the CGM into the intergalactic medium. The intergalactic medium represents the space outside the CGM and is defined as a sphere with radius equal to the virial radius of the dark matter halo that hosts the central galaxy. The mass of the CGM tends to increase if the mass of the dark matter halo also increases, as $\dot{M}_{CGM,in}$ can reach higher values due to a larger availability of gas in the environment; conversely, the CGM mass will decrease when the mass of the dark matter halo decreases, as gas can more efficiently leave the CGM, giving rise to higher values of $\dot{M}_{CGM,out}$. We can also decrease the mass of the gas in the CGM, even if the dark matter mass stays constant, by allowing the CGM to have large-scale outflows. Details of all of these terms can be found in Côté et al. (2018), Côté et al. (2019), and references therein [see fig. 7 of Côté et al. (2018) for a visual representation of the workings of OMEGA+].

The evolution of the galactic gas mass $\dot{M}_{gas}$ is defined as (Tinsley 1980; Pagel 1997; Matteucci 2012)

$$\dot{M}_{gas}(t) = \dot{M}_{inflow}(t) + \dot{M}_{ej}(t) - \dot{M}_{\star}(t) - \dot{M}_{outflow}(t), \quad (2)$$

where $\dot{M}_{inflow}$ is the mass added by galactic inflows from the CGM, $\dot{M}_{ej}$ is the mass added by stellar ejecta, $\dot{M}_{\star}$ is the mass locked away by star formation, and $\dot{M}_{outflow}$ is the mass lost by outflows into the CGM. This equation is used at each time-step to track the evolution of the galaxy across 13 Gyr.

The infall prescription of gas from the CGM into the galaxy we use here is a dual-infall model based on Chiappini, Matteucci & Gratton (1997). It combines two episodes of exponential gas inflow and is

---

[1]OMEGA+ is available online as part of the JINAPYCEE package (https://github.com/becot85/JINAPyCEE).

[2]OMEGA is available online as part of the NUPYCEE package (https://github.com/NuGrid/NUPYCEE).

Table 1. Parameter values of the model, where A_1, A_2, τ_1, τ_2, and t_{max} are all free parameters of equation (3). $\epsilon_\star$, the sfe, and $\tau_\star$, the star formation time-scale, are the free parameters of equation (4) and η, the mass loading factor, is the free parameter of equation (5). These values are equivalent to the values in the 'best' model of Côté et al. (2019).

Parameter	Value
A_1 ($M_\odot$ yr^{-1})	46
A_2 ($M_\odot$ yr^{-1})	5.9
τ_1 (Gyr)	0.8
τ_2 (Gyr)	7.0
t_{max} (Gyr)	1.0
$\epsilon_\star$	0.23
$\tau_\star$ (Gyr)	1.0
η	0.52

described as follows:

$$\dot{M}_{\mathrm{inflow}}(t) = A_1 \exp\left(\frac{-t}{\tau_1}\right) + A_2 \exp\left(\frac{t_{\mathrm{max}} - t}{\tau_2}\right), \tag{3}$$

where A_1, A_2, τ_1, τ_2, and t_{max} are free parameters, the values for which can be found in Table 1. A_1 and A_2 represent the normalization of the first and second infall events, respectively, τ_1 and τ_2 are the time-scales for mass accretion for the first and second infall, and t_{max} is the time of maximum contribution of the second gas accretion episode, which is zero for the first episode.

The star formation rate is defined as

$$\dot{M}_\star(t) = \frac{\epsilon_\star}{\tau_\star} M_{\mathrm{gas}}(t), \tag{4}$$

where $\epsilon_\star$ and $\tau_\star$ are the dimensionless star formation efficiency (sfe) and star formation time-scale, respectively. The outflow rate is proportional to the star formation rate and is defined as

$$\dot{M}_{\mathrm{outflow}}(t) = \eta \, \dot{M}_\star(t), \tag{5}$$

where η is the mass loading factor and controls the strength of the outflows. The values for $\epsilon_\star$, $\tau_\star$, and η can also be found in Table 1.

To calculate the mass of gas added by stellar ejecta, the contribution of every stellar population formed by time t is summed so that

$$\dot{M}_{\mathrm{ej}}(t) = \sum_j \dot{M}_{\mathrm{ej}}^j (M_j, Z_j, t - t_j), \tag{6}$$

where $\dot{M}_{\mathrm{ej}}^j$ is the mass ejected by the jth stellar population, M_j is the initial mass of the population, Z_j is the initial metallicity of the population, and $t - t_j$ is the age of the jth population at time t. The simple stellar populations (SSPs) are created at every time-step using SYGMA (Stellar Yields for Galactic Modelling Applications) (Ritter et al. 2018a). An SSP is defined as a population of stars with the same age and chemical composition, with the number of each type of star in the different evolutionary stages being weighted by an initial mass function (IMF). In this work, we adopt the IMF of Kroupa (2001). SYGMA includes ejecta from low- and intermediate-mass stars, massive stars, Type Ia supernovae (SNe Ia), and neutron star mergers and additional sources can also be added manually by the user. The ejecta from the SSPs are then instantaneously and uniformly mixed into the gas reservoir.

SNe Ia are modelled by assuming a power-law delay-time distribution (DTD) similar to that of Maoz & Mannucci (2012, see also Freundlich & Maoz 2021; Wiseman et al. 2021) in the form $t^{-\beta}$ with $\beta = 1$. The minimum delay time of SNe Ia is set by the lifetime of intermediate-mass stars used in the GCE calculation. For every SSP, at any time t, the DTD is multiplied by the fraction of progenitor

Table 2. Combination of yields used for the chemical evolution modelling in this work. Here, FRUITY = Cristallo et al. (2015), Mon. 1 = Lugaro et al. (2012) and Karakas & Lugaro (2016), Karakas et al. (2018), and Mon. 2 is the same as previous but with heavy elements included, and ATON = Ventura et al. (2013, 2014, 2018). L&C are the massive star yields of Limongi & Chieffi (2018), Nomoto are the yields of Nomoto et al. (2013), and Iwamoto are the SN1a yields of Iwamoto et al. (1999).

| Model name	AGB yields	Massive star yields	SN Ia yields
CLCmix	FRUITY	L&C V_{rot} = mix	Iwamoto
CLC000	FRUITY	L&C V_{rot} = 0 km s^{-1}	Iwamoto
CLC150	FRUITY	L&C V_{rot} = 150 km s^{-1}	Iwamoto
CLC300	FRUITY	L&C V_{rot} = 300 km s^{-1}	Iwamoto
Mon18LCmix	Mon. 1	L&C V_{rot} = mix	Iwamoto
MonLCmix	Mon. 2	L&C V_{rot} = mix	Iwamoto
MonLC300	Mon. 2	L&C V_{rot} = 300 km s^{-1}	Iwamoto
CNom	FRUITY	Nomoto	Iwamoto
VenLCmix	ATON	L&C V_{rot} = mix	Iwamoto

white dwarfs [$f_{\mathrm{WD}}(t)$] originating from stars in the mass range of 3–8 $M_\odot$ (see Ritter et al. 2018a, for more details). $f_{\mathrm{WD}}(t)$ smoothly evolves from 0 to 1 when the age of the SSP transits from the lifetime of an 8 $M_\odot$ star to the lifetime of a 3 $M_\odot$ star. The temporal evolution of the rate of SNe Ia is normalized such that 10^{-3} SNe occur per units of solar mass formed (see table 5 in Côté et al. 2016, for references). We use the solar abundances of Asplund et al. (2009) throughout, where the ^{19}F solar abundance is $\log\left[\epsilon\,(\mathrm{F})\right] = 4.56 \pm 0.30$.

3.1 Stellar yields

Nine combinations of yields have been used throughout this work and are laid out in Table 2. We explore the following options for our AGB yields: (i) the FUll-Network Repository of Updated Isotopic Tables & Yields (FRUITY) for AGB stars from Cristallo et al. (2015), which are available for metallicities $10^{-4} \leq Z \leq 2 \times 10^{-2}$ and masses in the range 1.3–6.0 $M_\odot$; (ii) the Monash AGB yields from Lugaro et al. (2012), Karakas & Lugaro (2016), and Karakas et al. (2018) with metallicities $10^{-4} \leq Z \leq 3 \times 10^{-2}$ and masses in the range 0.9–8.0 $M_\odot$; (iii) an extended version of the previous Monash yields that cover the same range of masses and metallicities as the previous set, where heavy elements (anything heavier than iron) are also included (Karakas & Lugaro 2016; Karakas et al. 2018); and finally, (iv) the AGB yields from Ventura et al. (2013, 2014, 2018) with metallicities $3 \times 10^{-4} \leq Z \leq 1.4 \times 10^{-2}$ and masses in the range 1.0–7.5 $M_\odot$.

We consider the two following options for our massive star yields:

(i) Set R of Limongi & Chieffi (2018), who developed stellar evolution models for massive stars by assuming three different initial rotation velocities as follows: $v_{\mathrm{rot}} = 300$ km s^{-1}, $v_{\mathrm{rot}} = 150$ km s^{-1}, and no rotation; all of these options will be explored in this work. For each rotational velocity, Limongi & Chieffi (2018) developed models with initial iron abundances [Fe/H] = 0, −1, −2, and −3 dex in the mass range 13–120 $M_\odot$. The chemical evolution models of Prantzos et al. (2018) assume a yield set that combines the massive star models of Limongi & Chieffi (2018) with different v_{rot} depending on metallicity, by assuming that lower metallicity stars rotate faster, on average, than higher metallicity stars, as illustrated in fig. 4 of Prantzos et al. (2018). A similar mixture of rotating massive star models that varies as a function of [Fe/H] will also be explored in this work. The logic for this combination comes about because Meynet & Maeder (1997) stated that in order to conserve angular momentum, low-metallicity stars must rotate faster as they are more compact.
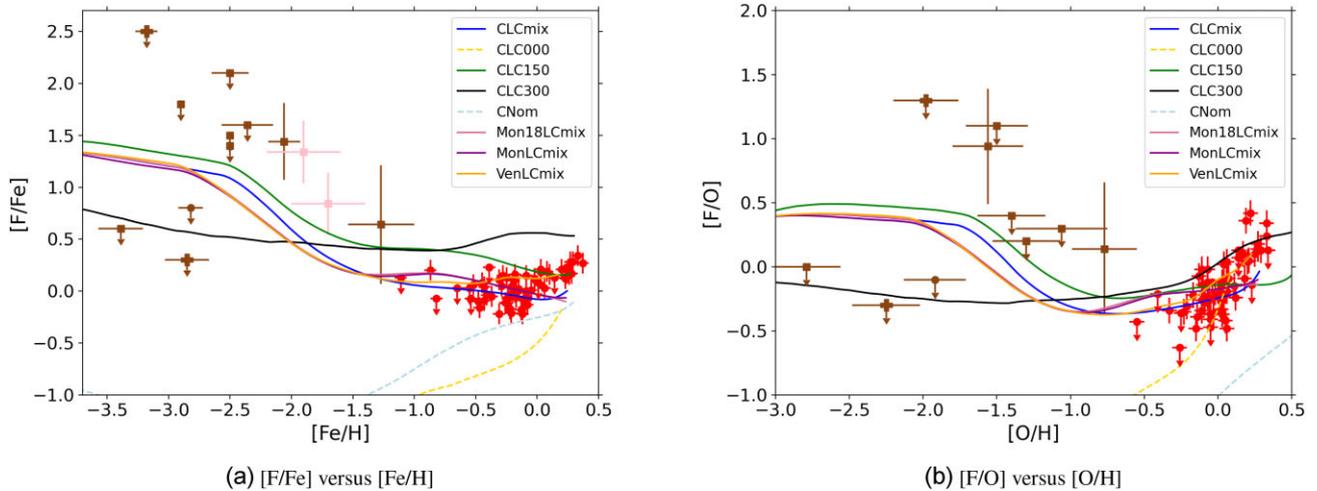
Figure 1. Left-hand panel: [F/Fe] versus [Fe/H] for models CLCmix, CLC000, CLC150, CLC300, CNom, Mon18LCmix, and MonLCmix. The red points are observations of fluorine from Ryde et al. (2020), the brown points from Lucatello et al. (2011), and the pink squares are Carina data from Abia et al. (2015). CEMP-s stars in the sample of Lucatello et al. (2011) are represented by brown squares, CEMP-no stars by brown crosses, and the carbon normal star by a brown point. Right-hand panel: the same but for [F/O] versus [O/H].

(ii) The yields of Nomoto, Kobayashi & Tominaga (2013; see also Kobayashi et al. 2006, 2011b, and Kobayashi, Karakas & Lugaro 2020) that do not include rotation. These yields use metallicities $10^{-3} \leq Z \leq 5 \times 10^{-2}$ in the mass range 13–40 $M_\odot$.

Of these yield sets, we mainly consider the FRUITY AGB yields because they cover a large range of masses and metallicities. The code used to calculate these yields is also coupled to a full nuclear network up to the termination point of the s-process; therefore, it considers the full range of isotopes and reactions relevant to this work. For massive stars, we mainly use the yields of Limongi & Chieffi (2018) in order to investigate the impact of rotation. Finally, for all models we use the W7 SNIa yields of Iwamoto et al. (1999).

4 RESULTS

Fig. 1(a) shows the abundance trend of [F/Fe] versus [Fe/H] for models assuming different combinations of yields, as summarized in Table 2. The predictions of our models are compared with high metallicity observations of fluorine abundances in the red giant sample of Ryde et al. (2020, red points with error bars) and low metallicity observations in red giants from Lucatello et al. (2011, brown square symbols represent stars classified as CEMP-s, whereas brown crosses are CEMP-no stars; the carbon normal star is represented by a brown point) and Abia et al. (2015, pink squares with error bars). We remind the readers that our models predict the evolution of the chemical abundances in the interstellar medium (ISM), hence how the birth abundances of stars change with time throughout the evolution of the Galaxy.

The two models that include massive stars with no rotation (CLC000 and CNom) show an increasing trend in [F/Fe] at higher metallicities that is in line with observations. However, these two models lie below the observed abundances. We note that, in the low-metallicity regime from $-3.5 <$ [Fe/H] < -2, the observational data are upper limits rather than absolute measurements, along with the high dispersion of the observational data in this metallicity range, which prevents us from drawing strong conclusions in this regime. The strongest constraint on our chemical evolution models is provided by observations in the metallicity range $-0.7 <$ [Fe/H] < 0.4.

We can still draw conclusions in the range $-2 <$ [Fe/H] < -0.7 but we are limited by poor statistics. All models with rotating massive stars included cut through the middle of the upper limits, with the majority of the brown points sitting above the chemical evolution trend lines. This is important because we know that an upper limit means that the value quoted has the potential to be lower than what is measured. We also see that the models including rotating massive stars are consistent with the bulk of the high-metallicity data. We note that models with higher v_{rot} can reach increasingly higher [F/Fe] ratios at high metallicity. None the less, no model with high v_{rot} reproduces the upward trend seen in observations at high [Fe/H], which is only seen in the models with $v_{rot} = 0$.

Fig. 1(b) shows the abundance trend of [F/O] versus [O/H] for the same set of models as in Fig. 1(a). These ratios are commonly plotted together when studying the chemical evolution of fluorine to trace the impact of the chemical enrichment from massive stars with minimal connection to the choice of the location of the mass cut in the massive star models. Looking at chemical evolution trends relative to oxygen is also useful because they do not include the uncertainties associated with SN Ia models. In Fig. 1(b), the trajectories are again compared with observations from Ryde et al. (2020) and Lucatello et al. (2011). Again, some observations provide better constraints for our GCE models than others, with those at [O/H] > -0.4 providing the strongest constraint. We can see that all models that include any sort of prescription for rotation in massive stars cut through the low metallicity observations, including VenLCmix. Further discussion of this model can be found later in the section. Of the two models that do not include rotating massive stars (CLC000 and CNom), only CLC000 reproduces the abundance trends of the high metallicity observations.

In Figs 1(a) and (b), we also investigate the impact of different AGB stellar yields on the chemical enrichment of fluorine. Our model with the FRUITY stellar yields for AGB stars (CLCmix) predicts similar abundance trends as the models with the Monash stellar yields (Mon18LCmix and MonLCmix). The model with the AGB stellar yields of Ventura et al. (2013, 2014, 2018) (VenLCmix) predicts higher final fluorine abundances in both Figs 1(a) and (b) compared to the FRUITY and Monash yields but they still lie within the high metallicity observations.
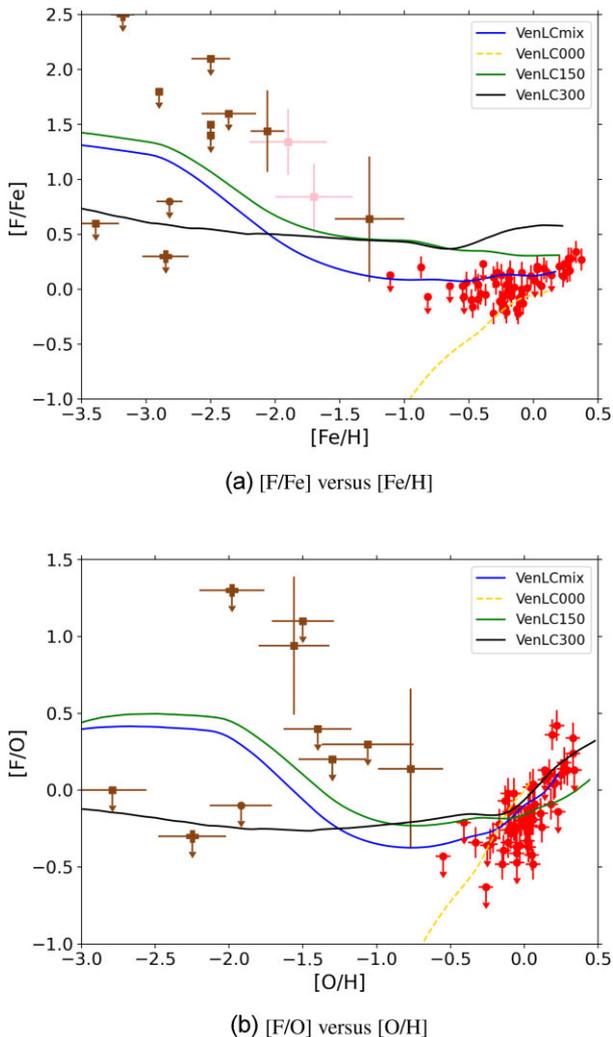
Figure 2. Panel a: [F/Fe] versus [Fe/H] for the Ventura et al. (2013, 2014, 2018) AGB yields in combination with each rotational prescription of the Limongi & Chieffi (2018) massive stars, compared with the same observational data as Fig. 1(a). Panel b: same as Fig. 2(a) but for [F/O] versus [O/H].

The AGB stellar yields of Ventura et al. (2013, 2014, 2018) are explored in more detail in Fig. 2, which shows chemical evolution models combining those yields with massive star models with different initial v_{rot} from Limongi & Chieffi (2018). Fig. 2(a) shows our results for [F/Fe] versus [Fe/H], whereas Fig. 2(b) focuses on [F/O] versus [O/H]. In each figure, the chemical evolution trends for each massive star prescription are similar in shape to the trends we predict when assuming the FRUITY AGB yields. However, the final values for models VenLCmix, VenLC000, VenLC150, and VenLC300 for both [F/Fe] and [O/H] are systematically higher than CLCmix, CLC000, CLC150, and CLC300.

The AGB stellar yields of Ventura et al. (2013, 2014, 2018) were the reference set adopted by Grisoni et al. (2020) in their 'parallel' chemical evolution model for the solar neighbourhood. However, when comparing our results with those in fig. 1 of Grisoni et al. (2020), we caution the readers that we assume a different IMF and DTD for SNe Ia. In particular, Grisoni et al. (2020) assumed the IMF of Kroupa, Tout & Gilmore (1993), which hosts much lower numbers of massive stars than the IMF of Kroupa (2001) that we use in our models (see also Vincenzo et al. 2016, for more details);

secondly, while Grisoni et al. (2020) assumed the SN Ia single-degenerate model of Matteucci & Recchi (2001), here we assume a power-law DTD that is motivated by recent observational surveys (see also Wiseman et al. 2021, for an observational perspective, and Vincenzo, Matteucci & Spitoni 2017, for the impact of those two different DTDs on elemental abundance trends; Maoz & Mannucci 2012).

When we consider the [F/Fe] versus [Fe/H] abundance diagram (Fig. 2a), our model with $v_{rot} = 0$ (VenLC000) predicts [F/Fe] ratios that are always ≈0.5 dex higher than model Thin-V000 of Grisoni et al. (2020). Our models with $v_{rot} = 150$ and 300 km s^{-1} (VenLC150 and VenLC300, respectively), instead, always lie below models Thin-V150 and Thin-V300 of Grisoni et al. (2020) for iron abundances between $-1.5 \lesssim$ [Fe/H] $\lesssim -0.5$ but then move above them as metallicity increases. It is difficult to compare models with variable v_{rot} because we follow different prescriptions. We recall that Grisoni et al. (2020) chose the prescription of Romano et al. (2019) with a sharp transition from $v_{rot} = 300$ to 0 km s^{-1} at [Fe/H] = -1 dex, whereas our model uses a prescription from Prantzos et al. (2018) that employs a more gradual change to lower rotational velocities as the metallicity increases. The mix of rotational velocities adopted in the present work (VenLCmix) follows the observational trends much more closely than Thin-Vvar of Grisoni et al. (2020).

When we consider the [F/O] versus [O/H] abundance diagram (Fig. 2b), our models with $v_{rot} = 0$ km s^{-1} always lie above model Thin-V000 of Grisoni et al. (2020), being separated by a constant offset of ≈0.2 dex. Our model VenLC150 appears to sit lower than Thin-V150 of Grisoni et al. (2020) for [Fe/H] $\lesssim 0$ dex. Interestingly, the models with $v_{rot} = 300$ km s^{-1} follow a very similar shape in both this work and Grisoni et al. (2020). However, our model always lies below Thin-V300 of Grisoni et al. (2020), being separated by an offset of ≈0.3 dex. Our model with a rotational mix (VenLCmix) can reproduce the observations at high metallicity more closely than the Thin-Vvar of Grisoni et al. (2020). However, we remind the reader once again that each of our works employs a different prescription for rotational mixing.

In summary, this discussion shows how careful we must be when we make chemical evolution models, and it further highlights the uncertainties we have in trying to best model the Milky Way.
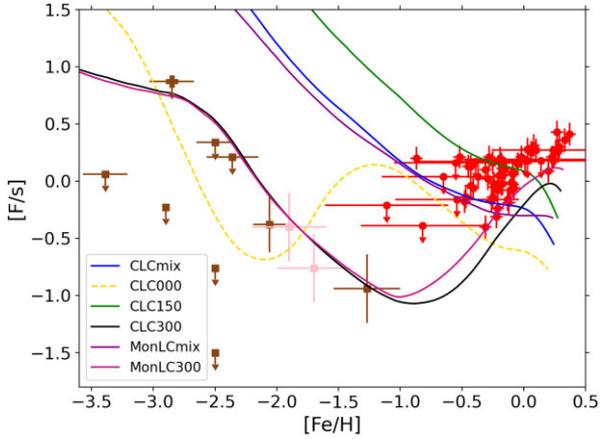
4.1 Fluorine and s-process elements

The interplay between fluorine and s-process elements has been previously commented on in the literature (e.g. Abia et al. 2011, 2015, 2019; Lucatello et al. 2011). Fluorine and s-process elements can be made together both in AGB stars and massive stars, especially when mixing is enhanced by rotation.

In massive stars, fluorine nucleosynthesis takes place in the helium convective shell via a series of reactions involving α-captures and proton captures. s-process elements in massive stars are synthesized via neutron captures, with the neutrons primarily coming from the ^{22}Ne (α, n) ^{25}Mg reaction. ^{22}Ne is synthesized from ^{14}N produced in the convective H-burning shell and brought into the He-burning core. Once in the core, two convective α-captures starting from ^{14}N produce ^{22}Ne. This process continues into the carbon burning phase (see Pignatari et al. 2010; Prantzos et al. 2018, for more details). In massive star models without rotation, we might expect to see s-process production up to the so-called first peak, i.e. Sr, Y, and Zr (e.g. Limongi & Chieffi 2003). However, Frischknecht, Hirschi & Thielemann (2012) showed that the efficiency of the mixing processes described above can be greatly enhanced within rapidly rotating massive stars, leading to s-process production beyond the first peak.
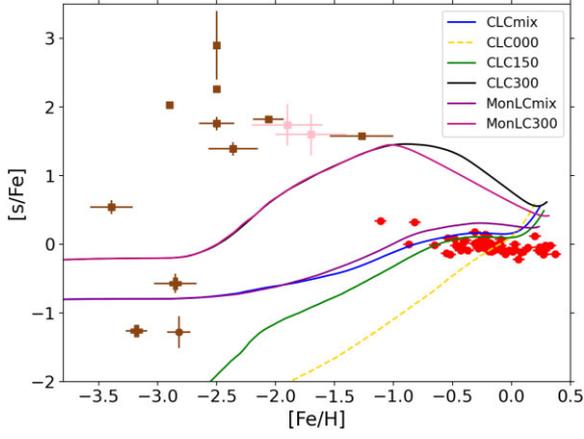
Figure 3. [s/Fe] versus [Fe/H] for models CLCmix, CLC000, CLC150, CLC300, MonLCmix, and MonLC300. The observational data are the same as Fig. 1(a).
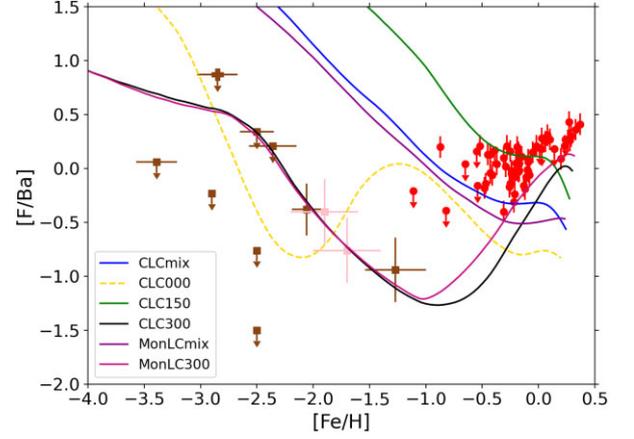

Figure 4. [F/s] versus [Fe/H] for models CLCmix, CLC000, CLC150, CLC300, MonLCmix, and MonLC300. The observational data are the same as Fig. 1(a).

In AGB stars, both fluorine and s-process elements are made during thermal pulses. Fluorine is made via a series of neutron, proton, and α captures that use ^{14}N as the seed nucleus. s-process elements are made via neutron captures in the intershell region of the star (e.g. Busso, Gallino & Wasserburg 1999). The primary neutron source here is the ^{13}C $(\alpha, n)\,^{16}$O reaction. Given the similar production sites of fluorine and s-process elements, it seems likely that where we find one we would likely find the other. This means that there is a potential correlation between fluorine and s-process elements that needs to be explored.

Fig. 3 shows the [s/Fe] versus [Fe/H] abundance trend for the models CLCmix, CLC000, CLC150, CLC300, MonLCmix, and MonLC300, which are specified in Table 2. The models with the AGB yields of Ventura et al. (2013), the first set of Monash AGB yields (Mon. 1), and the massive star yields of Nomoto et al. (2013) are not shown because they do not include heavy element abundances. In Figs 3 and 4, 's' denotes the average s-process abundance for each of the models, where [s/Fe] is defined as follows (Abia et al. 2002):

$$[s/Fe] = ([Sr/Fe] + [Y/Fe] + [Zr/Fe] + [Nb/Fe]$$
$$+ [Ba/Fe] + [La/Fe] + [Ce/Fe] + [Pr/Fe])/8.$$

Figure 5. [F/Ba] versus [Fe/H] for models CLCmix, CLC000, CLC150, CLC300, MonLCmix, and MonLC300. The observational data are the same as Fig. 1(a).

If we focus on the very low metallicity regime, the only models that can reproduce the high upper limits on [s/Fe] are those that include massive stars with $v_{\rm rot} = 300\,{\rm km\,s^{-1}}$. In the domain $-2.5 < [{\rm Fe/H}] < -1$, the models CLC300 and MonLC300 underestimate the observations. These models also severely overestimate [s/Fe] at high metallicity, disagreeing with the observations of Ryde et al. (2020). We note that a similar mismatch was also seen by Vincenzo et al. (2021) when comparing their models with the Limongi & Chieffi (2018) rotating massive star yields to the stellar abundance measurements of neutron-capture elements from the second data release of the GALactic Archaeology with HERMES (GALAH) survey (Buder et al. 2018). The rest of the models (those with a minor or absent contribution from stars with $v_{\rm rot} = 300\,{\rm km\,s^{-1}}$) provide a better explanation for the high metallicity observations, with CLCmix and CLC150 reproducing the plateau in the data up to solar metallicity.

Fig. 4 shows [F/s] versus [Fe/H] for the same models as Fig. 3. By investigating this ratio, we can continue to probe the chemical evolution of fluorine. For comparison, Fig. 5 shows [F/Ba] versus [Fe/H] for the same set of models. Since there is minimal change in the trajectory of the chemical evolution trends between [F/s] in Fig. 4 and [F/Ba] in Fig. 5, we can safely use the average s-process abundances for comparison with stellar observations by including a variety of s-process elements without loss of important information from tracking elements individually.

In the low-metallicity regime ($-3.4 < [{\rm Fe/H}] < -2.3$), the abundance of F and s-process elements for the CEMP stars in the figure has likely arisen due to accretion of material from an AGB companion (e.g. Busso et al. 2001; Sneden, Cowan & Gallino 2008; Lucatello et al. 2011; Mura-Guzmán et al. 2020). Coupled with the fact that most of the observations in this region are upper limits, we cannot use these observations to constrain the GCE models. That being said, it is noteworthy that two scenarios seem to provide similar predictions for [F/s] in Fig. 4: (i) AGB + massive stars with $v_{\rm rot} = 0$ (CLC000), and (ii) AGB + massive stars with $v_{\rm rot} = 300\,{\rm km\,s^{-1}}$ (CLC300 and MonLC300). These two scenarios are potentially very different. For stars rotating as quickly as $300\,{\rm km\,s^{-1}}$, the fluorine present on the surface will likely have been transported from the interior layers on to the surface due to the strong mixing from rotation. However, internal mixing is not as strong for non-rotating massive stars, so there may not be as much fluorine transported from the interior layers to the
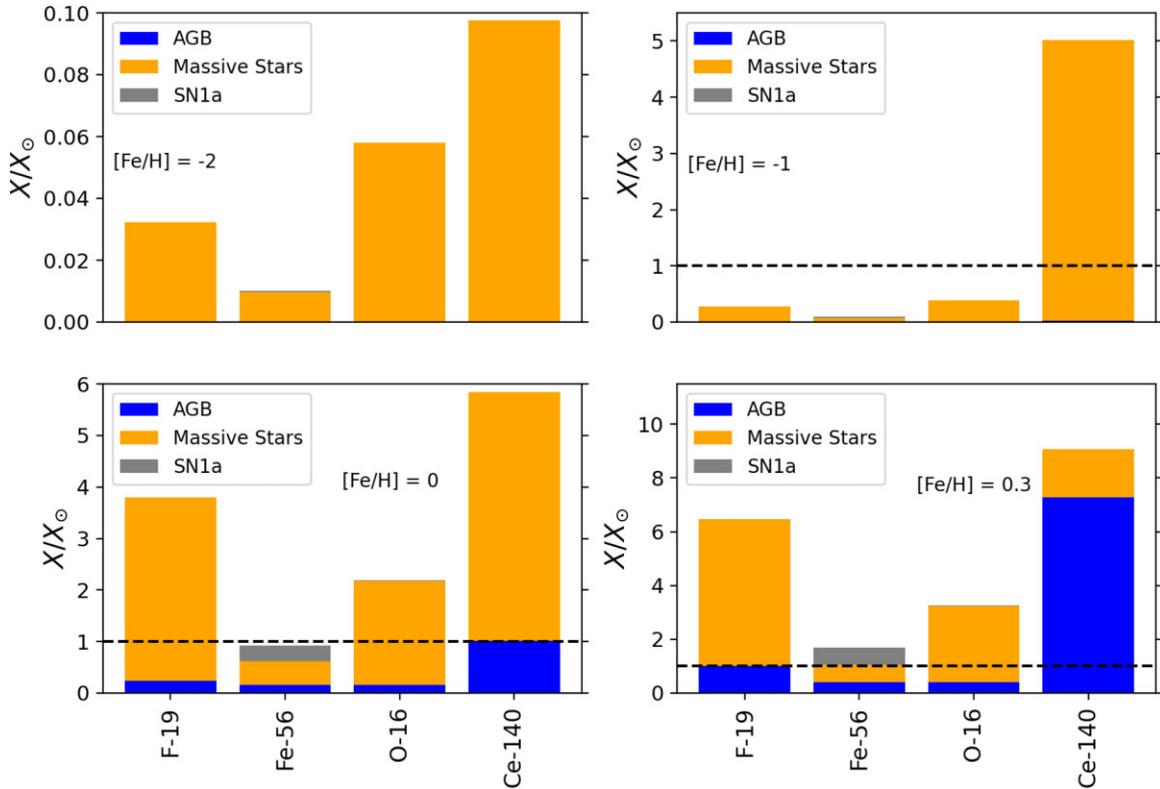
Figure 6. The contribution of each stellar source relative to solar for model CLC300 at metallicities [Fe/H] $= -2$ (top left), [Fe/H] $= -1$ (top right), [Fe/H] $= 0$ (bottom left), and [Fe/H] $= 0.3$ (bottom right – present). The contribution from massive stars is shown in orange, AGB stars in blue, and SNe 1a in grey.

surface. This could mean that some of the surface fluorine is present due to accretion from a companion.

There are two key details in the figures presented in this work that can separate the two potentially different scenarios mentioned above.

(i) In Fig. 4, the solar and supersolar metallicity observations from Ryde et al. (2020) show an upturn in their [F/s] that is only predicted by the models with $v_{\rm rot} = 300\,{\rm km\,s^{-1}}$.

(ii) In Fig. 1(a), model CLC000 is below all the observations, which means that solely including non-rotating massive stars is not enough to reproduce the observed fluorine abundance pattern.

Overall, this suggests that we need a contribution from rotating massive stars throughout the evolution of the Galaxy in order to reproduce the observations; in particular, Fig. 4 shows that massive stars with $v_{\rm rot} = 300\,{\rm km\,s^{-1}}$ might play a crucial role in the chemical evolution of fluorine, especially when considering the simultaneous production of s-process elements.

Figs 6 and 7 disentangle the contributions from massive stars, AGB stars, and Type Ia SNe to ^{19}F, ^{56}Fe, ^{16}O, and ^{140}Ce as predicted by the model with $v_{\rm rot} = 300\,{\rm km\,s^{-1}}$ (CLC300). Here, cerium is used as a proxy for the s-process elements. We can see that the massive star model with $v_{\rm rot} = 300\,{\rm km\,s^{-1}}$ dominates both ^{19}F and ^{140}Ce even when AGB stars kick in between $-1 < {\rm [Fe/H]} < 0$. Fig. 7 highlights this range in more detail.

By looking at the predictions of model CLC300 in Figs 6 and 7, both ^{19}F and ^{140}Ce abundances at [Fe/H] $= 0$ are higher than solar by a factor of ≈ 4 and ≈ 6, respectively (the black dashed line on each panel corresponds to the solar fluorine and cerium abundances). Therefore, even though models CLC300 and MonLC300 are best at reproducing the observational trends of Fig. 4, the fluorine and average s-process abundances that they generate at solar metallicity are not physical,

suggesting that a mix of massive star models with different $v_{\rm rot}$ should be assumed. The mix of rotational velocity we might expect will be discussed in the following section.

5 DISCUSSION

At low metallicity, most red giants in the sample of Lucatello et al. (2011) are classified as CEMP-s; hence, they likely had their surface fluorine abundances altered by binary mass transfer from an AGB companion. In Figs 1(a)–5, we also show CEMP-no stars, whose origin in the Milky Way halo is less clear. Our model predictions at low metallicity can solely be used as a baseline for the average ISM abundances at the point of birth of the stars, before any binary accretion has occurred, providing an empirical constraint on the degree of fluorine enhancement for AGB stellar models. There is also a larger spread in the observed chemical abundance patterns at [Fe/H] < -2.5, which indicates a more inhomogeneous ISM at low metallicity, as stars formed out of gas enriched by a smaller number of CCSNe, whereas our models assume that the ISM is well mixed at all times, with the IMF being fully sampled starting from the turn-off mass. An additional source of scatter in the chemical abundances at [Fe/H] < -2.5, which is not included in our models, might be due to the fact that the Milky Way halo comprises several populations of stars that were born in different substructures and were later accreted by our Galaxy. We also note again that the observations in the metallicity range $-3.4 < {\rm [Fe/H]} < -2.3$ are upper limits with a lot of dispersion. All this leads to uncertainty in our conclusions at [Fe/H] < -2.

At supersolar metallicity, there is a secondary behaviour of fluorine (Ryde et al. 2020). However, we must be careful about comparing our models to observations at this metallicity for a number of reasons.
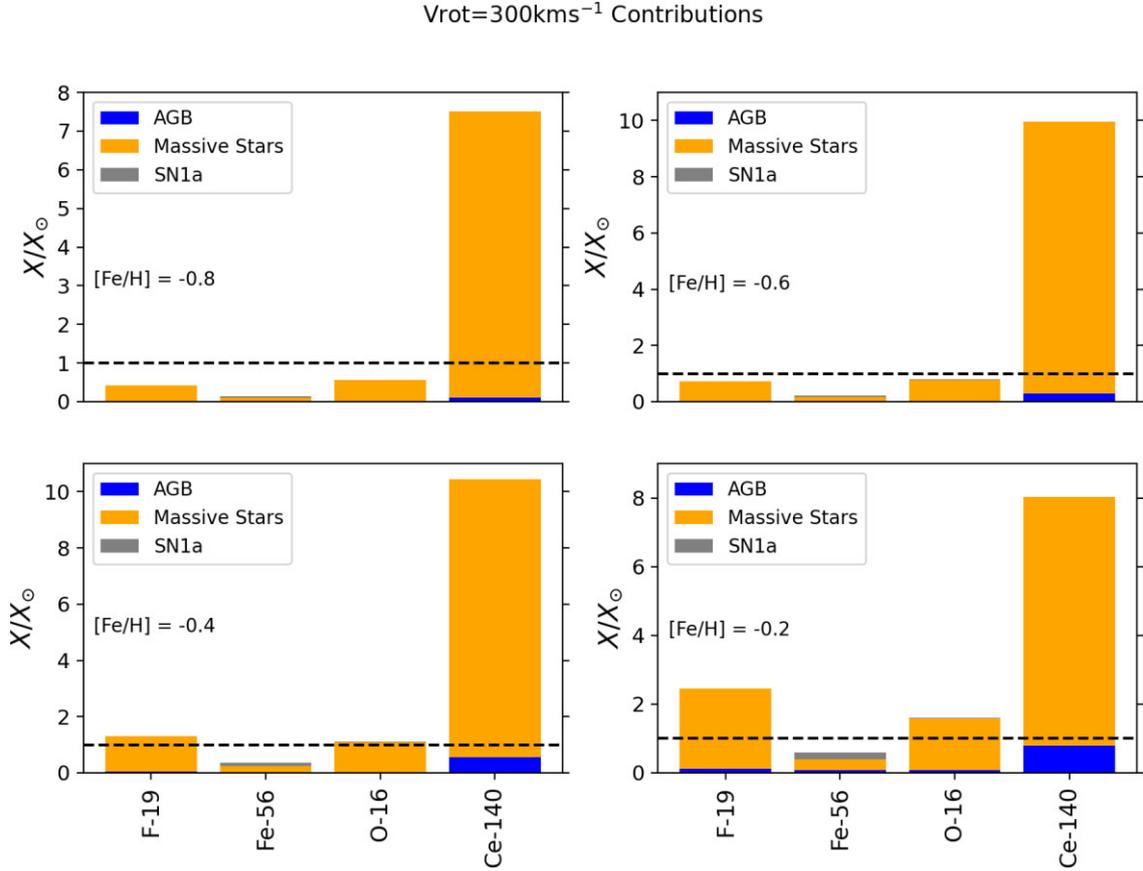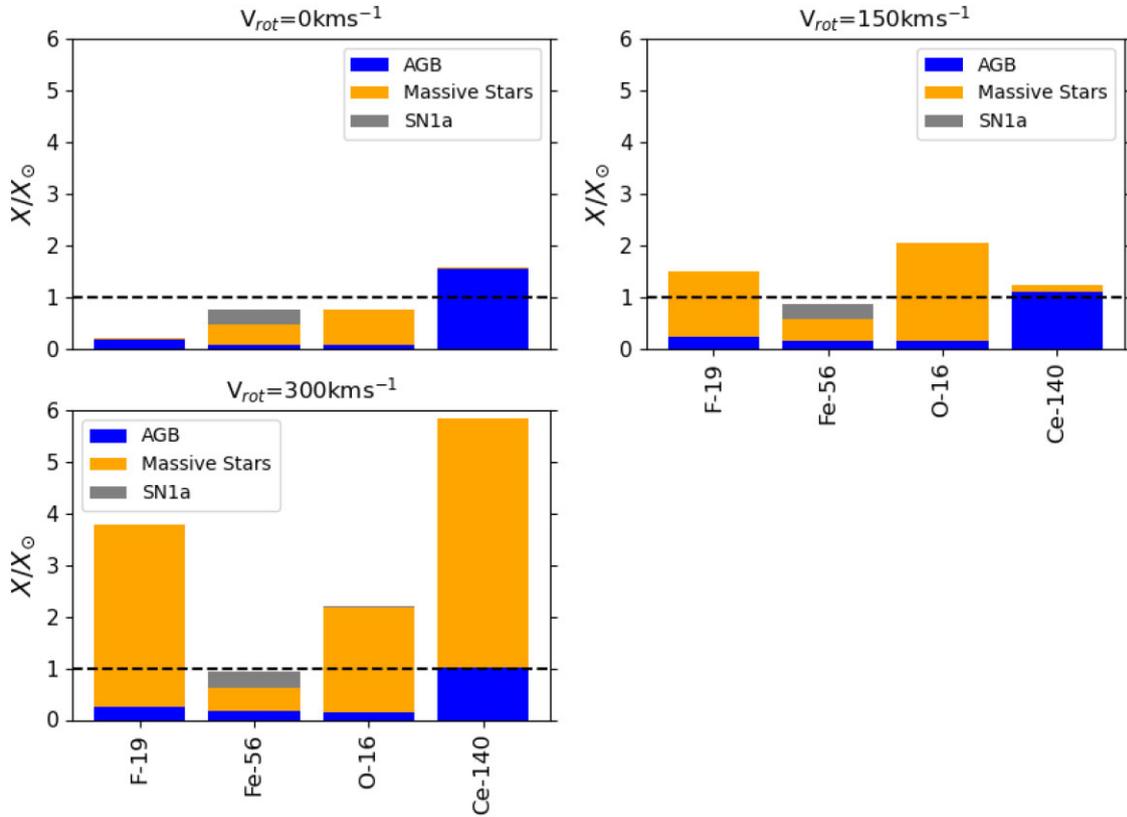
Figure 7. The contribution to each isotope from each stellar source relative to solar for model CLC300 at metallicities [Fe/H] = −0.8 (top left), [Fe/H] = −0.6 (top right), [Fe/H] = −0.4 (bottom left), and [Fe/H] = −0.2 (bottom right – present). The contribution from massive stars is shown in orange, AGB stars in blue, and SNe 1a in grey.

The first being that we do not have fluorine yields at supersolar metallicity; instead, at [Fe/H] > 0 the model copies the yields from the final metallicity until the end of the simulation (when the age of the galaxy is 13 Gyr). Secondly, stars with supersolar metallicity are known to have formed in the inner disc and migrated, so their composition is different to that of the local gas (see fig. 10 of Vincenzo & Kobayashi 2020, for an illustration of this). Therefore, the abundances of supersolar metallicity stars cannot be compared with a one-zone model. Though we do not make strong conclusions about the evolution of fluorine above [Fe/H] = 0, these considerations should be kept in mind.

The models using massive stars with initial rotational velocities of 300 km s^{-1} are the only ones to reproduce both the slight downward trend of [F/s] at low metallicity and upward trend of [F/s] at high metallicities. Therefore, we need a contribution from rapidly rotating massive stars with initial rotational velocities of 300 km s^{-1} throughout the evolution of the Galaxy in order to match the full abundance pattern. Though models CLC300 and MonLC300 do not match the full abundance trend of the observations in the [F/Fe] versus [Fe/H] space (Fig. 1a), there are many considerations to be made including the fact that the low metallicity observations are upper limits, so there is a chance that those observations could sit lower than where they are placed, and we expect fewer massive stars rotating that quickly at higher metallicities (see Meynet & Maeder 1997; Prantzos et al. 2018). Therefore, we should explore the possibility of a mix of initial rotational velocities, where stars with v_{rot} in the range 150–300 km s^{-1} contribute throughout the evolution

of the Galaxy. Romano et al. (2019) assumed a sharp transition for massive star rotation where massive stars have v_{rot} = 300 km s^{-1} for [Fe/H] < −1 and, suddenly, v_{rot} = 0 for [Fe/H] ≥ −1. This strategy is not appropriate for the situation we have here, as a contribution from models with v_{rot} in the range 150–300 km s^{-1} needs to be assumed even above [Fe/H] = −1. Given we know that at higher metallicities massive stars should rotate more slowly, perhaps a combination of rotational velocities is present at higher metallicities, much like the approach employed by Prantzos et al. (2018).

The mixed-rotation scenario of Prantzos et al. (2018) assumes that rotating massive stars with v_{rot} = 300 km s^{-1} cease to contribute to the yields at around [Fe/H] ≈ −2, failing to reproduce the observed trend of [F/s] as a function of [Fe/H] (see model CLCmix in Fig. 4). Therefore, a different combination of rotating massive star models needs to be employed, by including a metallicity-dependent contribution from models with v_{rot} = 150 and 300 km s^{-1} up to solar metallicity. Fig. 8 shows the contributions of each rotational velocity to the isotopes ^{19}F, ^{56}Fe, ^{16}O, and ^{140}Ce relative to solar for models CLC000, CLC150, and CLC300 at [Fe/H] = 0. Model CLC000 predicts $X(^{19}$F$)/X_{\odot}(^{19}$F$) = 0.2$ and $X(^{140}$Ce$)/X_{\odot}(^{140}$Ce$) = 1.5$, model CLC150 predicts $X(^{19}$F$)/X_{\odot}(^{19}$F$) = 1.4$ and $X(^{140}$Ce$)/X_{\odot}(^{140}$Ce$) = 1.2$, and model CLC300 predicts $X(^{19}$F$)/X_{\odot}(^{19}$F$) = 3.7$ and $X(^{140}$Ce$)/X_{\odot}(^{140}$Ce$) = 5.8$, at [Fe/H] = 0. In order to reproduce the fluorine solar abundance, we need to achieve $X(^{19}$F$)/X_{\odot}(^{19}$F$) = 1.0$. This can be done with a 45 per cent contribution from v_{rot} = 0 km s^{-1}, a 50 per cent contribution from v_{rot} = 150 km s^{-1},

Figure 8. The contribution to each isotope from each stellar source relative to solar at [Fe/H] = 0 for models CLC000 (top left), CLC150 (top right), and CLC300 (bottom). The contribution from massive stars is shown in orange, AGB stars in blue, and SNe 1a in grey.

and a 5 per cent contribution from $v_{rot} = 300 \, \mathrm{km \, s^{-1}}$. When employing these contributions, we achieve [F/Fe] = 0.08, [F/O] = −0.033, and [F/s] = −0.45. These percentage contributions are our suggestion for a mix of rotational velocities that are successful at reproducing fluorine abundances at solar metallicity. It is difficult to make a suggestion for combinations at other metallicities as we do not have a constraint for the abundances. We must be careful when suggesting a combination of rotational velocities as there are uncertainties in the yields that we must be aware of. First, a change in the implementation of rotation may change the yields of elements affected by rotation. As discussed by Prantzos et al. (2018), another uncertainty associated with the Limongi & Chieffi (2018) yields in particular is the enhancement of fluorine in the 15 and 20 $M_\odot$ models with $v_{rot} = 150 \, \mathrm{km \, s^{-1}}$. In these models, a smaller He convective shell forms separately to the main He convective shell. When these two shells merge, the base of the new shell is deeper and thus, is exposed to higher temperatures, which causes an enhancement in fluorine production. It is pointed out by Prantzos et al. (2018) that it is difficult to know whether this scenario is 'realistic' given it only affects two of the stellar models. Other uncertainties such as reaction rates and nuclear networks will be discussed later in this work.

It has been proposed that a contribution from novae is needed in order to match the observed behaviour of [F/O] versus [O/H] (e.g. Timmes et al. 1995; Spitoni et al. 2018). The majority of the models in this work (CLCmix, CLC150, CLC300, Mon18LCmix, and MonLCmix) can reproduce the trends of [F/O] versus [O/H] without including any chemical enrichment of fluorine from novae (see Fig. 1b). Therefore, it could be argued that we no longer need a contribution from novae to understand the chemical evolution of

fluorine. That being said, it is important to understand the fluorine yields we might expect from novae and the consequences that could have on our results. It is unclear from the literature both how frequent the occurrence of novae is and the fluorine yields we might get from them. Kawash et al. (2021) suggest a nova rate of ≈30 yr⁻¹, while Shafter (2017) suggests a nova rate of ≈50 yr⁻¹ and recent results from Rector et al. (2022) suggest a rate of ≈40 yr⁻¹; however, this result is for M31 rather than the Milky Way. Both Spitoni et al. (2018) and Grisoni et al. (2020) used the nova yields as predicted by Jose & Hernanz (1998), who found that fluorine is only significantly synthesized in their 1.35 $M_\odot$ model, with a maximum yield of $5.4 \times 10^{-5} \, M_\odot$ and a minimum yield of $9.9 \times 10^{-7} \, M_\odot$. This gives a range of potential ^{19}F nova production rate that varies between 2.97×10^{-5} and $2.7 \times 10^{-3} \, M_\odot \, \mathrm{yr^{-1}}$. The upper bound here is so high due to the significant yield from the 1.35 $M_\odot$ model. This wide range makes the contribution of novae to the galactic fluorine very uncertain. However, we can compare the potential nova yields to the yields we might expect from CCSNe. The CCSN rate is variable with time in our model with an average rate of 0.025 yr⁻¹. The minimum ^{19}F yield from the Limongi & Chieffi (2018) massive star yields with $v_{rot} = 300 \, \mathrm{km \, s^{-1}}$ is $1.027 \times 10^{-5} \, M_\odot$ and the maximum is $1.025 \times 10^{-3} \, M_\odot$. This yields a potential range of ^{19}F production rate from CCSNe between 2.57×10^{-7} and $2.56 \times 10^{-5} \, M_\odot \, \mathrm{yr^{-1}}$. This range is lower than that of the potential nova yields. However, we must be aware that only the 1.35 $M_\odot$ nova model is enhanced in fluorine, so there is the potential for the range of fluorine yield from novae to be lowered given that the enhancement only occurs at this one particular mass. Starrfield et al. (2020) looked at ^{19}F ejecta from novae for a 1.35 $M_\odot$ star and found a range of 6.3×10^{-11} to $1.0 \times 10^{-6} \, M_\odot$, again demonstrating how uncertain fluorine
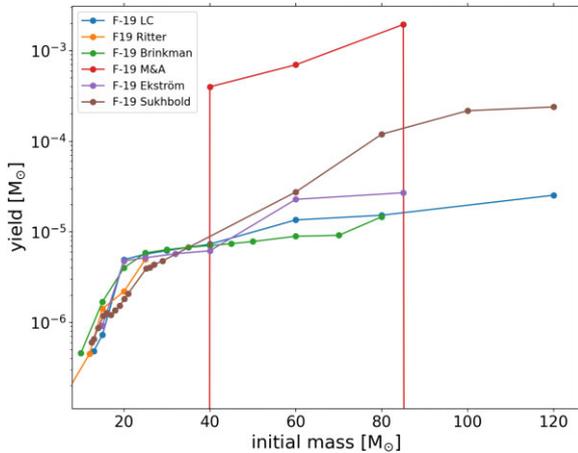
Figure 9. Non-rotating, solar metallicity wind yields from a range of studies over the last two decades. LC = Limongi & Chieffi (2018), Ritter = Ritter et al. (2018b), Brinkman = Brinkman et al. (2021), Brinkman (2022), M&A = Meynet & Arnould (2000), Ekström = Ekström et al. (2012), and Sukhbold = Sukhbold et al. (2016).
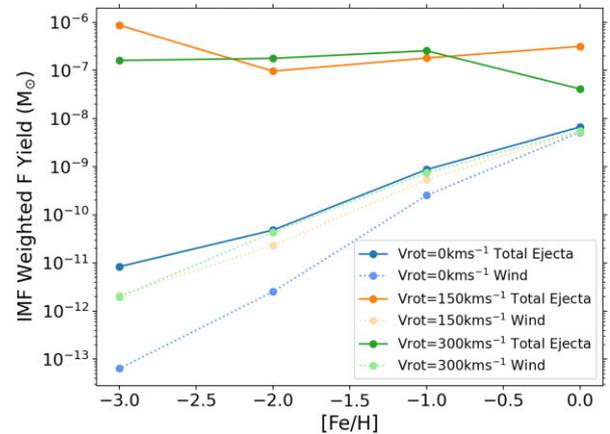

Figure 10. IMF-weighted fluorine yield as a function of metallicity ([Fe/H]) for each rotational velocity prescription. The total yields are shown by a full line and darker colour, while the wind yields are represented by dotted lines and lighter colours.

yields from novae can be. Overall, we recognize that novae may indeed contribute to the galactic fluorine, though the yields are highly uncertain and several critical assumptions need to be made to include them in chemical evolution models; however, they are not required to reproduce the observational abundance patterns in this work.

5.1 WR stars as a significant source of fluorine?

When massive stars rotate, they can, even if only for a brief period, enter into a WR phase. Given that WR winds have been suggested as a dominant contributor to the chemical evolution of fluorine (Meynet & Arnould 2000; Renda et al. 2004), it is important to disentangle what portion of the rotating massive star yields comes from WR winds and what portion comes from the CCSN at the end of their evolution.

Meynet & Arnould (2000) found that WR stars could contribute significantly to the galactic fluorine content by calculating a series of WR yields and incorporating them into a chemical evolution model for the Milky Way. They found that the ^{19}F wind yield of a $60\,M_\odot$ model could be a factor of 10–70 times higher than the initial stellar content of ^{19}F. These fluorine yields were subsequently used in the chemical evolution study of Renda et al. (2004), who explored three different scenarios for the nucleosynthesis of fluorine by using the chemical evolution code GETOOL (Fenner & Gibson 2003; Gibson et al. 2003). The first scenario explored by Renda et al. (2004) used solely yields from CCSNe, the second CCSNe and WR stars, and the third used CCSNe, WR, and AGB stars. Renda et al. (2004) concluded that, while AGB stars dominate fluorine production at low metallicity, WR stars are the dominant source of fluorine at solar and supersolar metallicities (see their fig. 4). In the years since, many more massive star models have been created that include WR yields. This begs the question, do any of these studies find ^{19}F yields as high as those found by Meynet & Arnould (2000)?

Fig. 9 shows a comparison of massive star wind yields from a variety of studies over the last couple of decades. The yields that are compared in the figure are from Limongi & Chieffi (2018), Ritter et al. (2018b), Brinkman et al. (2021), Brinkman (2022), Meynet & Arnould (2000), Ekström et al. (2012), and Sukhbold et al. (2016). Here, we look at non-rotating stars at solar metallicity in order to gain the widest comparison and to be able to compare with the non-rotating yields of Meynet & Arnould (2000). We can see that

all considered wind yields sit at least 1 dex below the Meynet & Arnould (2000) yields. This suggests that perhaps the Meynet & Arnould (2000) ^{19}F wind yields are unusually high compared to subsequent models. Therefore, there is potential that we may be able to rule out WR stars as a dominant contributor to the galactic fluorine budget.

To investigate this further, Fig. 10 shows the IMF-weighted yield versus metallicity for the Limongi & Chieffi (2018) massive star yields used in this work. Here, we see a comparison between the wind yield and the total ejecta for each rotational velocity. At low metallicity, the wind yields sit 4–6 dex lower than the total ejecta for the rotating models and around 2 dex lower for the non-rotating model. At higher metallicities, the gap between wind contribution and total ejecta reduces due to enhanced mass-loss, with the wind yields being around 2 dex lower than the total ejecta for the model rotating at $300\,\mathrm{km\,s^{-1}}$ and 1 dex lower for the model rotating at $150\,\mathrm{km\,s^{-1}}$. For the non-rotating model, the yields are almost identical at high metallicity.

We conclude that we need a large contribution from rapidly rotating massive stars in order to reproduce observations of fluorine in the Milky Way across the whole metallicity range. For $v_{\mathrm{rot}} = 300\,\mathrm{km\,s^{-1}}$, wind yields contribute a factor of around 10^{-2} less fluorine at high metallicities ([Fe/H] ≥ 0) and a factor of around 10^{-6} less fluorine at the lowest metallicity ([Fe/H] $= -3$) than the explosive yield, and for $v_{\mathrm{rot}} = 150\,\mathrm{km\,s^{-1}}$ wind yields contribute a factor of around 10^{-1} less fluorine at high metallicities and a factor of around 10^{-6} less fluorine at the lowest metallicity. We can therefore rule out WR stars as a dominant source of fluorine. Being able to draw such conclusions is vital in untangling the web of possibilities for the origin and chemical evolution of fluorine.

5.2 Sources of uncertainty in GCE

Like for any physical model, it is important to consider that there can be significant uncertainties concerning GCE studies (e.g. Romano et al. 2005, 2010). For example, each choice for the parameters in Table 1 can affect the behaviour of the chemical evolution models. Côté et al. (2016) explored some sources of GCE uncertainty, including the IMF, DTD and number of SNe Ia, current stellar mass, and star formation history.

We briefly explored the effect of changing both the IMF and the sfe of the models on our results. We found that

(i) using a Kroupa et al. (1993) IMF rather than Kroupa (2001) does not drastically change the results of the chemical evolution trends. Using the Kroupa et al. (1993) IMF produces more fluorine at lower metallicities, which can produce a slightly better fit for [F/Fe] versus [Fe/H] trends but provides an overproduction of [F/O] as a function of [O/H] for the models that use the Limongi & Chieffi (2018) yields. However, a better fit to the observations is achieved by the model including the massive star yields of Nomoto et al. (2013).

(ii) using a higher sfe naturally exhausts the available gas more quickly, and thus does not produce as much fluorine at higher metallicities, whereas a lower sfe sees a late increase in [F/Fe]. However, the shape of the chemical evolution trend is not significantly affected.

Another major source of uncertainty in GCE studies is the yield sets used (see e.g. Gibson 1997; Mollá et al. 2015). Each author will use a different code for stellar modelling, which will in turn use a different reaction network. A reaction network specifies the reactions that will occur in a model and the rates at which such reactions will occur. Different modelling choices made by each author produce a layered effect when it comes to the uncertainty provided by stellar yields in chemical evolution modelling.

To better understand reaction rate uncertainties in the context of this work, we will look at the two reactions that can destroy fluorine: $^{19}F(\alpha, p)^{22}Ne$ and $^{19}F(p, \alpha)^{16}O$.

(i) The most recent work on $^{19}F(p, \alpha)^{16}O$ was performed by Zhang et al. (2021b). By reanalysing experimental data, they found drastically different $^{19}F(p, \alpha)^{16}O$ rates than those recommended by the Nuclear Astrophysics Compilation of Reaction Rate (Angulo et al. 1999). They found rates larger by factors of 36.4, 2.3, and 1.7 for temperatures 0.01, 0.05, and 0.1 GK, respectively. This increased rate naturally leads to the destruction of ^{19}F on a scale larger than previously thought. By performing a network calculation at solar metallicity with their recommended new rate for the reaction, the value of ^{19}F decreased by up to one order of magnitude. This reaction was directly measured by Zhang et al. (2021a) using the Jinping Underground Nuclear Astrophysics experimental facility. Though the rate they found was 0.2–1.3 times lower than that of their theoretical prediction (Zhang et al. 2021b), it is still significantly higher than the accepted rate of Spyrou et al. (2000). Therefore, we will still expect a larger depletion of fluorine at solar metallicity using this reaction rate.

(ii) The most recent work to study $^{19}F(\alpha, p)^{22}Ne$ is Palmerini et al. (2019), who focused on the role that this reaction takes in AGB stars in particular. They found that during thermal pulses, ^{19}F can be easily destroyed by α-captures; in particular, for a $5\,M_\odot$ AGB star ^{19}F can be destroyed by a factor of 4.

These new discoveries related to the reactions that destroy fluorine could have implications for this work. If indeed, the destruction of fluorine is more enhanced in AGB stars than previously thought, the chemical evolution of fluorine at higher metallicities could be affected. The point at which AGB stars begin to be significant is model dependent. For model CLC300, Fig. 6 shows us that AGB stars begin to be significant in the production of fluorine around solar metallicity. Therefore, we might expect that the [F/Fe], [F/O], and [F/s] ratios studied in this work decrease from [Fe/H] = 0. Whether these reaction rates will also have a significant impact in the destruction of fluorine in rotating massive stars remains to be seen.

Uncertainties around reaction rates are a large source of uncertainty in stellar modelling and the yields we retrieve from those models. All this must be kept in mind when studying GCE. Given especially how uncertain each source's contribution to the galactic fluorine is, uncertainties around reaction rates add another piece to this complex puzzle.

6 CONCLUSIONS

We have studied the chemical evolution of fluorine in the Milky Way. We have used a range of yield sets to try to understand the dominant contributor to the galactic fluorine budget. In order to do this, we compared our chemical evolution models to abundance determinations across a wide range of metallicities. The main conclusions of this work are as follows:

(i) We investigated many combinations of yields with different prescriptions for the rotation of massive stars. Though we are limited by upper limits and poor statistics in the low-metallicity regime, we found that in order to reproduce fluorine abundances across the whole metallicity range ($-3.4 <$ [Fe/H] < 0.4), we need a contribution from rapidly rotating massive stars with initial rotational velocities as high as $300\,\text{km}\,\text{s}^{-1}$. We agree with the results of Prantzos et al. (2018) and Grisoni et al. (2020) that rotating massive stars play a crucial role in the fluorine production up to solar metallicities. We also suggest a combination of initial rotational velocities that can reproduce solar abundances.

(ii) We have investigated the contribution of massive star and WR winds to the galactic fluorine budget. We compared the winds of more recent massive star models to the winds of Meynet & Arnould (2000) and found that we expect to see significantly less fluorine in wind yields than we did 20 yr ago.

(iii) From the initial study of wind yields, we then looked at the fluorine yields from the winds of the massive stars used in our chemical evolution models. We found that the wind yield can be up to six times lower than the ejecta from the core collapse. Thus, we have ruled out WR winds as a dominant contributor to the galactic fluorine.

(iv) We can rule out novae as an important source of galactic fluorine. Our models can successfully reproduce the observational pattern in [F/O] versus [O/H] space and as thus we do not need a contribution from novae that others required in order to reproduce the pattern.

(v) These conclusions, especially those related to the low-metallicity regime, could be made stronger by additional observations of fluorine at low metallicity.

To conclude, our study into the chemical evolution of fluorine in the Milky Way has found that rapidly rotating massive stars are the dominant contributor to fluorine. We still need a contribution from AGB stars from [Fe/H] ≈ -1. We have now been able to rule out WR stars and novae as a significant contributor to the chemical evolution of fluorine.

DATA AVAILABILITY

The data generated for this article will be shared on reasonable request to the corresponding author.

REFERENCES

Abia C. et al., 2002, ApJ, 579, 817
Abia C., Cunha K., Cristallo S., Laverny P. D., Domínguez I., Recio-Blanco A., Smith V. V., Straniero O., 2011, ApJ, 737, 6
Abia C., Cunha K., Cristallo S., Laverny P. D., 2015, A&A, 581, A88
Abia C., Cristallo S., Cunha K., Laverny P. D., Smith V. V., 2019, A&A, 625, 1
Angulo C. et al., 1999, Nucl. Phys. A, 656, 3
Aoki W., Norris J. E., Ryan S. G., Beers T. C., Ando H., 2002, ApJ, 576, L141
Asplund M., Grevesse N., Sauval A. J., Scott P., 2009, ARA&A, 47, 481
Beers T. C., Christlieb N., 2005, ARA&A, 43, 531
Bisterzo S., Gallino R., Straniero O., Cristallo S., Käppeler F., 2010, MNRAS, 404, 1529
Brinkman H., 2022, PhD thesis, Univ. Szeged
Brinkman H. E., den Hartogh J. W., Doherty C. L., Pignatari M., Lugaro M., 2021, ApJ, 923, 47
Buder S. et al., 2018, MNRAS, 478, 4513
Busso M., Gallino R., Wasserburg G. J., 1999, ARA&A, 37, 239
Busso M., Gallino R., Lambert D. L., Travaglio C., Smith V. V., 2001, ApJ, 557, 802
Chiappini C., Matteucci F., Gratton R., 1997, ApJ, 477, 765
Chiappini C., Hirschi R., Meynet G., Ekström S., Maeder A., Matteucci F., 2006, A&A, 449, L27
Choplin A., Hirschi R., Meynet G., Ekström S., Chiappini C., Laird A., 2018, A&A, 618, A133
Côté B., Ritter C., O'Shea B. W., Herwig F., Pignatari M., Jones S., Fryer C. L., 2016, ApJ, 824, 82
Côté B., O'Shea B. W., Ritter C., Herwig F., Venn K. A., 2017, ApJ, 835, 128
Côté B., Silvia D. W., O'Shea B. W., Smith B., Wise J. H., 2018, ApJ, 859, 67
Côté B., Yagüe A., Világos B., Lugaro M., 2019, ApJ, 887, 213
Cristallo S., Leva A. D., Imbriani G., Piersanti L., Abia C., Gialanella L., Straniero O., 2014, A&A, 570, A46
Cristallo S., Straniero O., Piersanti L., Gobrecht D., 2015, ApJS, 219, 40
Cunha K., Smith V. V., 2005, ApJ, 626, 425
Cunha K., Smith V. V., Lambert D. L., Hinkle K. H., 2003, AJ, 126, 1305
Danilovich T. et al., 2021, A&A, 655, A80
de Laverny P., Recio-Blanco A., 2013, A&A, 555, A121
Ekström S. et al., 2012, A&A, 537, A146
Fenner Y., Gibson B. K., 2003, PASA, 20, 189
Forestini M., Goriely S., Jorissen A., Arnould M., 1992, A&A, 261, 157
Franco M. et al., 2021, Nat. Astron., 5, 1240
Freundlich J., Maoz D., 2021, MNRAS, 502, 5882
Frischknecht U., Hirschi R., Thielemann F.-K., 2012, A&A, 538, L2

Gibson B. K., 1997, MNRAS, 290, 471
Gibson B. K., Fenner Y., Renda A., Kawata D., Lee H.-c., 2003, PASA, 20, 401
Goriely S., Jorissen A., Arnould M., 1989, in Hillebrandt W., Müller E., eds, Proceedings of the 5th Workshop on Nuclear, Nuclear Astrophysics. MPIA, Munich, p. 60
Grisoni V., Spitoni E., Matteucci F., Recio-Blanco A., de Laverny P., Hayden M., Mikolaitis Ŝ., Worley C. C., 2017, MNRAS, 472, 3637
Grisoni V., Romano D., Spitoni E., Matteucci F., Ryde N., Jönsson H., 2020, MNRAS, 498, 1252
Guerço R., Ramírez S., Cunha K., Smith V. V., Prantzos N., Sellgren K., Daflon S., 2022, ApJ, 929, 24
Hampel M., Stancliffe R. J., Lugaro M., Meyer B. S., 2016, ApJ, 831, 171
Hansen C. J. et al., 2016a, A&A, 588, A37
Hansen T. T., Andersen J., Nordström B., Beers T. C., Placco V. M., Yoon J., Buchhave L. A., 2016b, A&A, 586, A160
Iwamoto K., Brachwitz F., Nomoto K., Kishimoto N., Umeda H., Hix W. R., Thielemann F., 1999, ApJS, 125, 439
Jönsson H., Ryde N., Spitoni E., Matteucci F., Cunha K., Smith V., Hinkle K., Schultheis M., 2017, ApJ, 835, 50
Jorissen A., Smith V., Lambert D., 1992, A&A, 261, 164
Jose J., Hernanz M., 1998, ApJ, 494, 680
Karakas A., Lattanzio J. C., 2007, PASA, 24, 103
Karakas A. I., Lugaro M., 2016, ApJ, 825, 26
Karakas A. I., Lugaro M., Carlos M., Cseh B., Kamath D., García-Hernández D. A., 2018, MNRAS, 477, 421
Kawash A. et al., 2021, ApJ, 922, 25
Kobayashi C., Umeda H., Nomoto K., Tominaga N., Ohkubo T., 2006, ApJ, 653, 1145
Kobayashi C., Karakas A. I., Umeda H., 2011a, MNRAS, 414, 3231
Kobayashi C., Izutani N., Karakas A. I., Yoshida T., Yong D., Umeda H., 2011b, ApJ, 739, 2
Kobayashi C., Karakas A. I., Lugaro M., 2020, ApJ, 900, 179
Kroupa P., 2001, MNRAS, 322, 231
Kroupa P., Tout C. A., Gilmore G., 1993, MNRAS, 262, 545
Lanfranchi G. A., Matteucci F., Cescutti G., 2006, A&A, 453, 67
Li H. N., Ludwig H. G., Caffau E., Christlieb N., Zhao G., 2013, ApJ, 765, 51
Limongi M., Chieffi A., 2003, ApJ, 592, 404
Limongi M., Chieffi A., 2018, ApJS, 237, 13
Lucatello S., Tsangarides S., Beers T. C., Carretta E., Gratton R. G., Ryan S. G., 2005, ApJ, 625, 825
Lucatello S., Masseron T., Johnson J. A., Pignatari M., Herwig F., 2011, ApJ, 729, 40
Lugaro M., Ugalde C., Karakas A. I., Gorres J., Wiescher M., Lattanzio J. C., Cannon R. C., 2004, ApJ, 615, 934
Lugaro M., Karakas A. I., Stancliffe R. J., Rijs C., 2012, ApJ, 747, 2
Maiorca E., Uitenbroek H., Uttenthaler S., Randich S., Busso M., Magrini L., 2014, ApJ, 788, 149
Maoz D., Mannucci F., 2012, PASA, 29, 447
Matteucci F., 1986, MNRAS, 221, 911
Matteucci F., 2012, Chemical Evolution of the Galaxy. Springer, Berlin
Matteucci F., Recchi S., 2001, ApJ, 558, 351
Meynet G., Arnould M., 2000, A&A, 355, 176
Meynet G., Maeder A., 1997, A&A, 321, 465
Mollá M., Cavichia O., Gavilán M., Gibson B. K., 2015, MNRAS, 451, 3693
Mura-Guzmán A., Yong D., Abate C., Karakas A., Kobayashi C., Oh H., Chun S. H., Mace G., 2020, MNRAS, 498, 3549
Nault K. A., Pilachowski C. A., 2013, AJ, 146, 153
Nomoto K., Kobayashi C., Tominaga N., 2013, ARA&A, 51, 457
Olive K. A., Vangioni E., 2019, MNRAS, 490, 4307
Pagel B. E. J., 1997, Nucleosynthesis and Chemical Evolution of the Galaxies. Cambridge Univ. Press, Cambridge
Palacios A., Arnould M., Meynet G., 2005, A&A, 443, 243
Palmerini S., D'Agata G., Cognata M. L., Indelicato I., Pizzone R. G., Trippella O., Vescovi D., 2019, J. Phys.: Conf. Ser., 1308, 012016
Pignatari M., Gallino R., Heil M., Wiescher M., Käppeler F., Herwig F., Bisterzo S., 2010, ApJ, 710, 1557

Prantzos N., Abia C., Limongi M., Chieffi A., Cristallo S., 2018, MNRAS, 476, 3432

Rector T. A. et al., 2022, ApJ, 936, 117

Renda A. et al., 2004, MNRAS, 354, 575

Ritter C., Côté B., Herwig F., Navarro J. F., Fryer C. L., 2018a, ApJS, 237, 42

Ritter C., Herwig F., Jones S., Pignatari M., Fryer C., Hirschi R., 2018b, MNRAS, 480, 538

Romano D., Chiappini C., Matteucci F., Tosi M., 2005, A&A, 430, 491

Romano D., Karakas A. I., Tosi M., Matteucci F., 2010, A&A, 522, A32

Romano D., Matteucci F., Zhang Z. Y., Ivison R. J., Ventura P., 2019, MNRAS, 490, 2838

Ryde N. et al., 2020, ApJ, 893, 37

Saberi M., Khouri T., Velilla-Prieto L., Fonfría J. P., Vlemmings W. H. T., Wedemeyer S., 2022, A&A, 663, A54

Shafter A. W., 2017, ApJ, 834, 196

Smith V. V., Cunha K., Ivans I. I., Lattanzio J. C., Campbell S., Hinkle K. H., 2005, ApJ, 633, 392

Sneden C., Cowan J. J., Gallino R., 2008, ARA&A, 46, 241

Spitoni E., Matteucci F., Jönsson H., Ryde N., Romano D., 2018, A&A, 612, A16

Spyrou K., Chronidou C., Harissopulos S., Kossionides S., Paradellis T., Rolfs C., Schulte W., Borucki L., 2000, Eur. Phys. J. A, 7, 79

Stancliffe R. J., Lugaro M., Ugalde C., Tout C. A., Görres J., Wiescher M., 2005, MNRAS, 360, 375

Starkenburg E., Shetrone M. D., McConnachie A. W., Venn K. A., 2014, MNRAS, 441, 1217

Starrfield S., Bose M., Iliadis C., Hix W. R., Woodward C. E., Wagner R. M., 2020, ApJ, 895, 70

Straniero O., Gallino R., Cristallo S., 2006, Nucl. Phys. A, 777, 311

Sukhbold T., Ertl T., Woosley S. E., Brown J. M., Janka H.-T., 2016, ApJ, 821, 38

Timmes F. X., Woosley S. E., Weaver T. A., 1995, ApJS, 98, 617

Tinsley B. M., 1980, Fundam. Cosm. Phys., 5, 287

Ventura P., Di Criscienzo M., Carini R., D'antona F., 2013, MNRAS, 431, 3642

Ventura P., Di Criscienzo M., D'Antona F., Vesperini E., Tailo M., Dell'Agli F., D'Ercole A., 2014, MNRAS, 437, 3274

Ventura P., Karakas A., Dell'Agli F., García-Hernández D. A., Guzman-Ramirez L., 2018, MNRAS, 475, 2282

Vincenzo F., Kobayashi C., 2020, MNRAS, 496, 80

Vincenzo F., Matteucci F., Vattakunnel S., Lanfranchi G. A., 2014, MNRAS, 441, 2815

Vincenzo F., Matteucci F., Belfiore F., Maiolino R., 2016, MNRAS, 455, 4183

Vincenzo F., Matteucci F., Spitoni E., 2017, MNRAS, 466, 2939

Vincenzo F., Thompson T. A., Weinberg D. H., Griffith E. J., Johnson J. W., Johnson J. A., 2021, MNRAS, 508, 3499

Wiseman P. et al., 2021, MNRAS, 506, 3330

Woosley S. E., Haxton W. C., 1988, Nature, 334, 45

Yong D., Meléndez J., Cunha K., Karakas A. I., Norris J. E., Smith V. V., 2008, ApJ, 689, 1020

Yoon J. et al., 2016, ApJ, 833, 20

Zhang L. Y. et al., 2021a, Phys. Rev. Lett., 127, 152702

Zhang L. Y., López A. Y., Lugaro M., He J. J., Karakas A. I., 2021b, ApJ, 913, 51

This paper has been typeset from a TeX/LaTeX file prepared by the author.